SCIENCE CHINA
Earth Sciences

A new method to constrain shallow crustal S-wave velocities based on direct P-wave amplitudes in receiver functions and its application in northeastern Tibet

Xu WANG, Ling CHEN, Yuan LING, Yifan GAO, Jianyong ZHANG and Huajian YAO

Citation: SCIENCE CHINA Earth Sciences; doi: 10.1007/s11430-018-9443-6

View online: http://engine.scichina.com/doi/10.1007/s11430-018-9443-6

Published by the Science China Press

SCIENCE CHINA
Earth Sciences

•RESEARCH PAPER•

https://doi.org/10.1007/s11430-018-9443-6

A new method to constrain shallow crustal S-wave velocities based on direct P-wave amplitudes in receiver functions and its application in northeastern Tibet

Xu WANG[1,3], Ling CHEN[1,2,3*], Yuan LING[1,3], Yifan GAO[1,3], Jianyong ZHANG[1,3] & Huajian YAO[4,5]

[1] *State Key Laboratory of Lithospheric Evolution, Institute of Geology and Geophysics, Chinese Academy of Sciences, Beijing 100029, China;*
[2] *CAS Center for Excellence in Tibetan Plateau Earth Sciences, Beijing 100101, China;*
[3] *University of Chinese Academy of Sciences, Beijing 100049, China;*
[4] *Laboratory of Seismology and Physics of Earth's Interior and School of Earth and Space Sciences, University of Science and Technology of China, Hefei 230026, China;*
[5] *Mengcheng National Geophysical Observatory, University of Science and Technology of China, Mengcheng 233500, China*

Received August 30, 2018; revised July 3, 2019; accepted July 16, 2019; published online September 18, 2019

Abstract A new method is developed to constrain S-wave velocity structures of the shallow crust based on frequency-dependent amplitudes of direct P-waves in P-wave receiver functions (P-RFs). This method involves the following two steps: first, the high-frequency approximate amplitude formula of direct P-waves in P-RFs of individual stations is used to fit the observed amplitude distribution against the ray parameters at different frequencies, and second, the S-wave velocity depth profile beneath each station is constrained according to an empirical correlation between frequency and depth. Unlike traditional inversion techniques, the newly developed method is not dependent on initial velocity models, and the lateral and vertical resolutions of the results are controlled by the interstation distance and the data frequency, respectively. The effectiveness of the method is verified by synthetic tests on various models. The method is then applied to teleseismic P-RF data from a NW-SE-trending linear seismic array extending from the northeastern Tibetan Plateau to the central Sichuan Basin to construct an S-wave velocity image of the shallow crust along the array. The imaged velocity structure is further analysed and compared with the regional geology. In particular, the structural differences of sedimentary basins in the cratonic area of the stable Sichuan Basin and tectonically active belts in northeastern Tibet are investigated. By combining our results with previous observations, the relationship between the surficial geology and deep processes in the study region is also discussed.

Keywords Receiver function, Direct P-wave amplitude, S-wave velocity structure, Shallow crust, Northeastern Tibet, Sichuan Basin

Citation: Wang X, Chen L, Ling Y, Gao Y, Zhang J, Yao H. 2019. A new method to constrain shallow crustal S-wave velocities based on direct P-wave amplitudes in receiver functions and its application in northeastern Tibet. Science China Earth Sciences, 62, https://doi.org/10.1007/s11430-018-9443-6

1. Introduction

Studies on velocity structures of the shallow crust can provide prior information for theoretical modelling and are also essential for the evaluation of exploration prospects and comparative studies of regional tectonics. For example, in regions such as cratons and tectonically active belts, velocity structures in the shallow crust can provide seismological constraints on sedimentary characteristics of basin-mountain systems and can improve the understanding of the relation-

* Corresponding author (email: lchen@mail.iggcas.ac.cn)

ship between surface deformation and deep processes. Located in southwestern Mainland China, the Sichuan Basin and the Tibetan Plateau represent an ancient stable craton and an active Phanerozoic orogen, respectively, which initially collided during the Triassic Indo-Sinian orogeny. The continental collision between the Indian and the Eurasian plates during the Cenozoic resulted in the extremely high topography and material extrusion of the Tibetan Plateau, which was obstructed by the rigid Sichuan Basin (Clark and Royden, 2000; Tapponnier et al., 2001; Yin and Harrison, 2000). The crust of eastern Tibet has been obviously thickened and severely deformed (Guo et al., 2013; Wang et al., 2011; Zhang et al., 2009), and the lithosphere has also probably been disrupted (Zhang et al., 2010). Because of its ~200-km-thick lithosphere with seismically fast velocities, the Sichuan Basin is considered to have remained rigid and stable and retained the characteristics of a typical craton (Zhang et al., 2018; Lei and Zhao, 2016). In this complex tectonic region where deep structures and deformation characteristics are drastically different, studies on velocity structures in the shallow crust are of significance for understanding the uplift of eastern Tibet and are essential for the prediction and assessment of seismic and geologic hazards and the exploration of energy resources, such as geothermal energy.

Seismic exploration and geophysical logging are two commonly used methods to study the shallow crustal structures. Velocity structures determined by the two methods are of high resolution because of the mature technologies and because logging can directly measure or sample deep-seated materials. However, seismic exploration and logging technologies are usually not suitable for studying crustal structures at the regional scale because of their high expense and their general application only to exploration targets. In recent years, with the rapid development of broadband seismic observations, inversions based on Rayleigh wave vertical-horizontal amplitude ratios (Arai and Tokimatsu, 2004; Yuan et al., 2016) and/or ambient noise surface wave dispersion data (Fang et al., 2015) to constrain shallow structures have become more popular. In this study, we develop a new method that uses frequency-dependent amplitudes of direct P-waves in the (teleseismic radial) P-wave receiver functions (P-RFs) for seismic imaging of shallow crustal structures. The new method is an extended application of P-RFs as well as a good method for jointly inverting shallow structures with surface wave data.

A P-RF is a time series that contains the conversions (Ps) and multiples (PpPs, PsPs+PpSs) from crustal and upper mantle discontinuities; thus, it can be used to determine the deep structures inside the Earth. Most existing P-RF methods use the conversions and/or multiples to constrain the depth, shape and physical properties of discontinuities (e.g., Ai et al., 2003; Bostock and Rondenay, 1999; Chen et al., 2005a, 2005b, 2006; Dueker and Sheehan, 1997; Yang et al., 2018; Zhu and Kanamori, 2000), although few studies have focused on the direct P phases, especially the amplitudes (Liu et al., 1996; Ammon et al., 1990; Owens et al., 1984; Zheng et al., 2006). Despite the consideration of direct P phases, traditional inversions generally suffer from nonunique solutions, because of their strong dependence on initial models. In addition, conversions from near-surface discontinuities are usually merged with direct P phases on account of the relatively low main frequencies of the teleseismic data. Therefore, traditional inversion methods based on a single frequency receiver function have difficulty constraining shallow structures. The results from analytical formulation and numerical simulation under conditions of high-frequency approximation suggest that direct P-wave amplitudes in P-RFs are sensitive to near-surface S-wave velocities (Julià, 2007). This relationship has been used to study the near-surface S-wave velocity structures in northeastern Tibet (Qian et al., 2018). However, theoretical analysis and practical application remain lacking regarding the application of frequency-dependent amplitudes of P-RF direct P-waves to quantitatively constrain velocity variations with depth.

Based on theoretical analysis and simulation, in this study, we obtain an empirical correlation between the observed frequency of the direct P-waves in the P-RFs and the depth they mainly reflect and discuss the feasibility of using their multi-frequency amplitudes to study shallow crustal velocity variations with depth. Then, a high-resolution velocity image of the shallow crust of eastern and northeastern Tibet and the adjacent Sichuan Basin is constructed using teleseismic P-RF data from a NW-SE-trending linear seismic array. This array was deployed by the Institute of Geology and Geophysics, Chinese Academy of Sciences in 2010–2013 (see details in Section 3). Along with previous observations, the newly shown variations in near-surface velocity structures and sedimentary features in this study as well as their possible relations to deep processes are discussed.

2. Method and theoretical simulations

Given a horizontally layered isotropic model, the direct P-wave amplitude in a P-RF under the high-frequency approximation can be expressed as follows (Julià, 2007):

$$A_{\mathrm{P}p} = \frac{r_{\mathrm{P}p}}{z_{\mathrm{P}p}} = \frac{2p\eta_{V_{\mathrm{S}_0}}}{1/V_{\mathrm{S}_0}^2 - 2p^2}, \quad (1)$$

where $r_{\mathrm{P}p}$, $z_{\mathrm{P}p}$, and p are the radial amplitude, the vertical amplitude and the ray parameter (i.e., horizontal slowness) of incoming P-waves, respectively; V_{S_0} is the near-surface S-wave velocity; and $\eta_{V_{\mathrm{S}_0}} = (1/V_{\mathrm{S}_0}^2 - p^2)^{1/2}$ is the vertical slowness. The amplitudes of direct P-waves in P-RFs ($A_{\mathrm{P}p}$)

are only related to the ray parameters and near-surface S-wave velocities in the ideal case. The ray parameter can be determined by knowing the coordinates of an earthquake hypocenter and recording station for a global velocity model, under which the amplitude is only related to the S-wave velocity. Thus, the near-surface S-wave velocity can be deduced by the magnitudes of the direct P-wave amplitudes in P-RFs.

Eq. (1) for direct P-wave amplitudes is derived in terms of the high-frequency approximation. In real data processing, P-RFs are generated by deconvolving vertical components from radial components in either the time domain or the frequency domain. In the frequency domain, the division is sometimes unstable because of the presence of near-zero values in the vertical component. Therefore, a water level, which controls the accuracy of the receiver functions, is introduced to reduce the instability. In addition, the calculation in the frequency domain is based on the assumption that values outside of the time window are zero or periodic, leading to the resolution of results being strongly influenced by the length and sample rate of the data. Unlike the frequency domain method, the time domain maximum entropy deconvolution method considers the maximum entropy as an extrapolation criterion for regions outside of the window, which improves the resolution of the receiver functions (Wu and Zeng, 1998; Wu et al., 2003). In this study, both the synthetic and observed receiver functions are extracted using the time domain maximum entropy deconvolution method.

To determine how the amplitudes change with both S-wave velocities and ray parameters, two one-dimensional (1-D) velocity models were established. The two models have the same crystalline crust and upper mantle but a different velocity of the sedimentary cover: 2.4 km s^{-1} for the low-velocity model and 3.3 km s^{-1} for the high-velocity model. The P-wave velocity and density in each layer are defined as V_P=1.77V_S and ρ=0.32V_P+0.77, respectively (hereinafter all models refer to these relations). The seismograms are predicted for the models by the reflectivity method (Kennett, 1983), and then, P-RFs are extracted with different Gaussian factors and ray parameters (Figure 1a and 1b). For the real data, the calculation of P-RFs introduces a Gaussian filter ($e^{-\frac{\omega^2}{4\alpha^2}}$) to suppress high-frequency noise. Here, we define the frequency when the filter amplitude drops to 1/e as the highest effective frequency:

$$f_c \approx \alpha/\pi. \quad (2)$$

Synthetic receiver functions with different ray parameters and different Gaussian factors for the low-velocity model (black line in the inset of Figure 1c) are shown in Figure 1a and 1b, respectively. Given either a ray parameter or S-wave velocity, the results indicate that the direct P-wave amplitudes increase with the other. Simulated amplitudes of direct P-waves based on the low-velocity and high-velocity models (inset in Figure 1c) are shown as black and red crosses in Figure 1c, and the best-fit S-wave velocities based on eq. (1) are 2.411 and 3.326 km s^{-1}, respectively. The direct P-wave amplitudes can be used to constrain the near-surface S-wave velocity under the high-frequency approximation, although the velocities derived from the direct P-wave amplitudes are slightly different from the true values. The discrepancy (<1%) may result from calculation errors during the deconvolution.

Eq. (1) is tenable only under the assumption that wavelets in the receiver functions are delta (δ) functions, i.e., the time series consists of infinitely high-frequency components. However, receiver functions are calculated within a limited frequency band; thus, the direct P-wave amplitudes merely represent values within a limited frequency range. The direct P-wave amplitudes vary (Figure 1b); thus, the derived velocities change with the observed frequencies.

To intuitively describe the frequency-dependence characteristics of the direct P-wave amplitudes, we established three models: uniform-, positive-gradient-, and stepped-type models. The three models have the same mantle structure with an S-wave velocity of 4.2 km s^{-1} and the same crustal thickness of 45 km. The simulated amplitudes of direct P-waves for the three models are shown in Figure 1d–1f. For the uniform-type model, the amplitudes do not change with frequency (Figure 1d), whereas the amplitudes for the positive-gradient-type model (Figure 1e) and stepped-type model (Figure 1f) increase with decreasing frequencies but to different degrees. This result suggests that variations in the direct P-wave amplitudes with frequency represent structures from the surface down to different depths; that is, amplitudes at relatively high frequencies reflect velocity structures near the surface, while low-frequency amplitudes reflect those from the surface to a greater depth.

The vertical extent of the velocity structures that dominate the direct P-wave amplitudes is closely related to the P-wave wavelength near the surface. A previous study discussed the dependence of reflection and transmission coefficients on the thickness of the 660-km discontinuity (Bostock, 1999). The results showed that the PP transmission coefficients increase with increasing thickness and reach a maximum when the discontinuity thickness is approximately half the P-wave wavelength, after which the transmission coefficients remain constant. Thus, the transmission waves may be sensitive to velocity structures within approximately one-half a wavelength; hence, the direct P-waves are dominated by structures from the surface to approximately $\lambda_P/2$ depth. Accordingly, the direct P-wave amplitudes at different frequencies can be used to constrain depth-dependent velocity structures beneath a station. For models in which the shallow structures are uniform, the P-wave wavelength at a given Gaussian factor can be determined as follows:

$$\lambda_P \approx \kappa\pi V_S/\alpha, \quad (3)$$

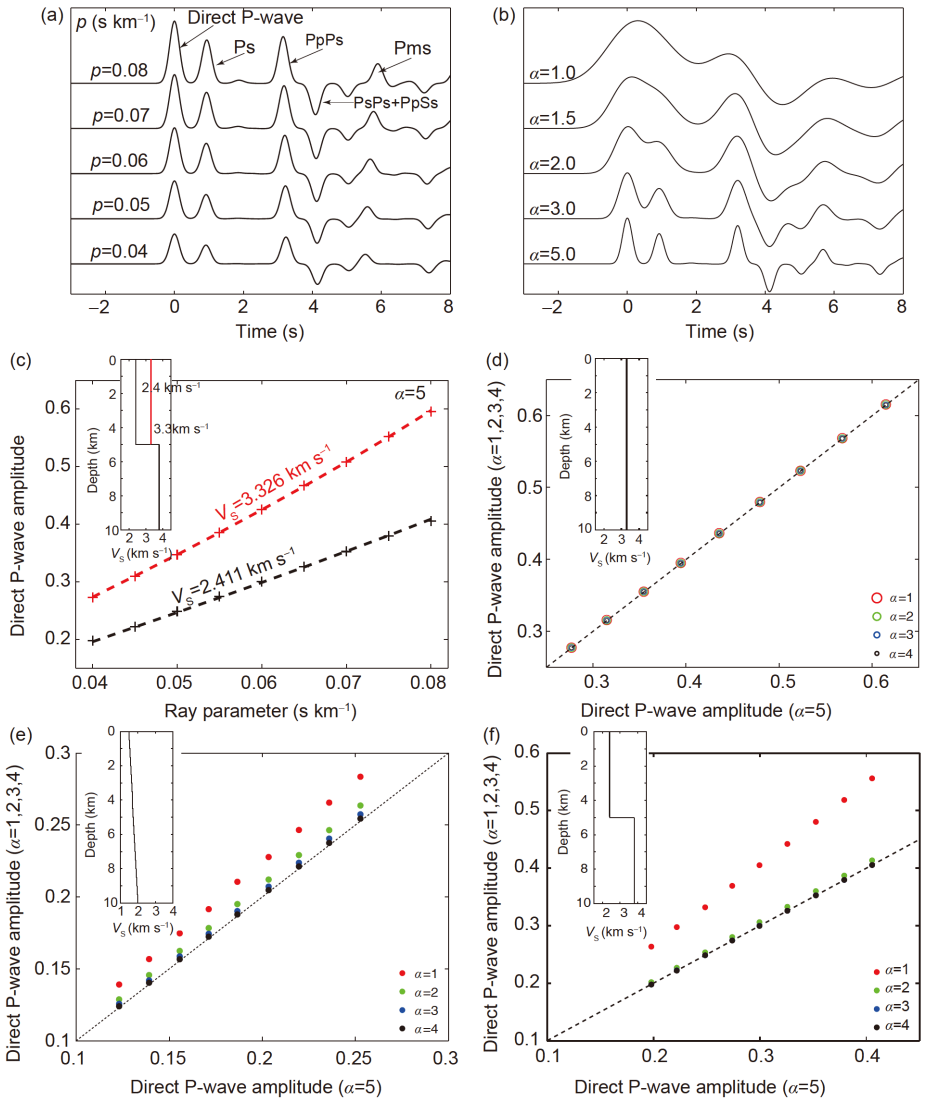

Figure 1 Variations of direct P-wave amplitudes with ray parameters and frequencies. (a), (b) Synthetic receiver functions based on the low-velocity model (black line in the inset of (c)) with different ray parameters (α=5.0) and different Gaussian factors (p=0.06 s km^{-1}). In (a), Ps, PpPs and PsPs+PpSs represent the first converted phase and two multiple phases from the shallow discontinuity; Pms represents the conversion from the Moho. Insets in (c)–(f) show synthetic models. In (c), the black and red crosses represent the simulated amplitudes of direct P-waves with a Gaussian factor of 5.0, the black and red dashed lines represent the best-fit curves according to eq. (1), and the corresponding S-wave velocity is noted on the line. In (d)–(f), the red, green, blue and black dots represent the direct P-wave amplitudes with Gaussian factors of 1.0, 2.0, 3.0, and 4.0, respectively (ordinate axis); amplitudes with a Gaussian factor of 5.0 are shown for comparison (abscissa axis).

$$h = \lambda_P / 2. \quad (4)$$

In eq. (3), κ represents the V_P/V_S ratio. Generally, the P- and S-wave velocities vary with depth; thus, the wavelengths are also depth dependent. For each station, we averaged all S-wave velocities at different frequencies to estimate the P-wave wavelength and initially established a model by setting the velocity at a specific frequency based on half the corresponding wavelength (eqs. (3) and (4)). Subsequently, the depths were optimized by improving wavelength estimation based on a travel-time-weighted velocity (crosses in Figure 2). We tested the performance of the empirical correlation between frequency and depth in resolving different structures. The results suggest that velocity structures can be recovered well for positive-gradient-type models, and, despite some deviations near the interface, the major features of stepped-type models are also well resolved. The velocity derived by the direct P-wave amplitude represents the depth-integrated product of velocities because the amplitudes at individual periods are sensitive to a broad depth range. As a result, the method based on frequency-depth conversion is less sensitive to sharp discontinuities (Figure 2b).

3. Real data processing

The teleseismic data used in this study originate from a NW-

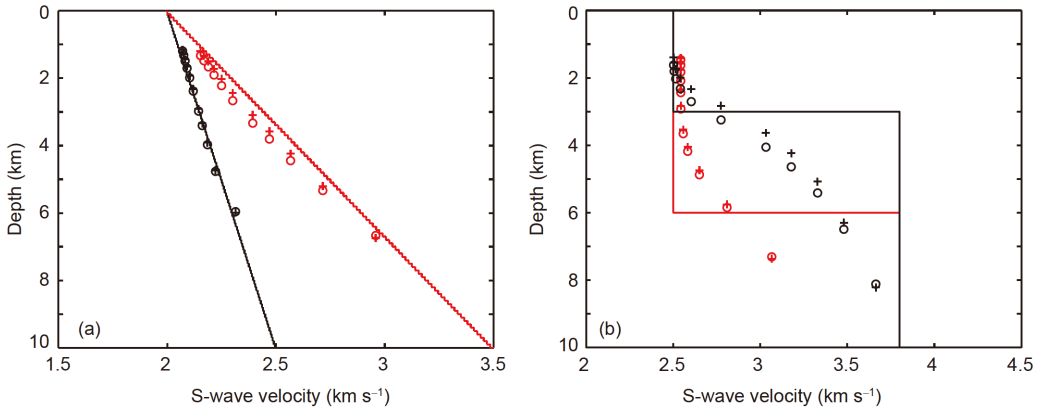

Figure 2 Models recovered based on the empirical correlation between frequency and depth ((a), positive-gradient-type model; (b), stepped-type model). The red and black solid lines represent the synthetic models, the red and black circles represent the models recovered based on the mean velocities at all frequencies used, and the red and black crosses are the optimized models according to the travel-time-weighted velocities based on the initially recovered models.

SE-trending linear array that consists of 64 broadband seismic stations with an interval of 10–15 km. As shown in Figure 3a and 3b, the seismic array starts in the northwest at the southern margin of the Qilian Orogen, crosses the Gonghe Basin in the Kunlun-Qaidam terrane and the Ruoergai Basin in the Songpan-Ganzi terrane, and terminates in the southeast within the central Sichuan Basin. Twenty-four stations on the easternmost side were operated from November 2010 to November 2012, and the others were operated from September 2012 to September 2013. Three-component seismograms with high signal-to-noise ratios were selected from 1009 events with magnitudes ≥5.5 and epicentral distances between 28° and 92° (Figure 3c). Despite uneven back-azimuth distributions, the events have good coverage for epicentral distances, ensuring a good database for this study. The waveforms were windowed from 20 s before to 100 s after the P-wave arrival to calculate the P-RFs (with a water level of 0.001). In total, 14237 P-RFs were selected, ensuring that the direct P-waves are clear and the Ps conversions from the Moho are clearly visible. For the twenty-four stations on the easternmost side, ~350 P-RFs were used at each station, and for the others, ~150 P-RFs were used. The P-RFs have been previously applied to post-stack migration imaging of the crustal structure along the seismic array (Wang et al., 2018). In this study, the direct P-wave amplitudes in the P-RFs were used to constrain the S-wave velocity in the shallow crust.

To obtain the velocity depth profile of the shallow crust, 11 Gaussian factors (1.0, 1.25, 1.5, 1.75, 2.0, 2.5, 3.0, 3.5, 4.0, 4.5, and 5.0, with frequencies of 0.32, 0.40, 0.48, 0.56, 0.64, 0.80, 0.95, 1.11, 1.27, 1.43, and 1.60 Hz, respectively) commonly used for studying the crustal structure were chosen to calculate the P-RFs. At some of the stations, the direct P-waves in the P-RFs may be contaminated by phases from shallow discontinuities. The extraction of the direct P-wave amplitudes was therefore performed as follows:

(1) All maxima within a certain time window (−1 to 2 s) were selected. If there was no maximum, the receiver function was discarded; otherwise, the maximum of all maxima was temporarily defined as the amplitude of the direct P-wave y.

(2) It was then determined whether there was a maximum point x before the temporarily defined amplitude y. If one did not exist, the amplitude was set to y; otherwise, the minimum value between y and x was used in the next step.

(3) If the minimum value was less than a certain ratio of x (0.8 in this study), x was redefined as the amplitude of the direct P-wave y.

(4) Steps (2) and (3) were repeated until no maximum existed before y.

The direct P-wave amplitudes from two stations with markedly different frequency-dependence characteristics are shown in Figure 4a and 4b (see Figure 3b for station locations). At station s167, amplitudes change gradually with frequency, reflecting a uniform velocity structure in the northern Ruoergai Basin. In contrast, with decreasing frequency, the amplitudes at station s188 increase significantly, indicating that the velocities increase rapidly with depth beneath the Gonghe Basin.

To reduce the influence of an uneven epicentral distance distribution, we defined a residual error in terms of the ray parameter density (eq. (5)). Specifically, the ray parameter space was divided into several subspaces, and the differences between the observed and synthetic amplitudes in each subspace were averaged using inverse-variance weighting. The subspace length was controlled by a minimum number of data points in each subspace (10 in this study).

$$\delta = \sum_{j=1}^{M} \frac{1}{N_j \sigma_j} \sum_{i=1}^{N_j} \left| F_{i,j}(V_{S_0}, p_{i,j}) - y_{i,j} \right|, \tag{5}$$

where M and N_j are the subspace number and P-RF number

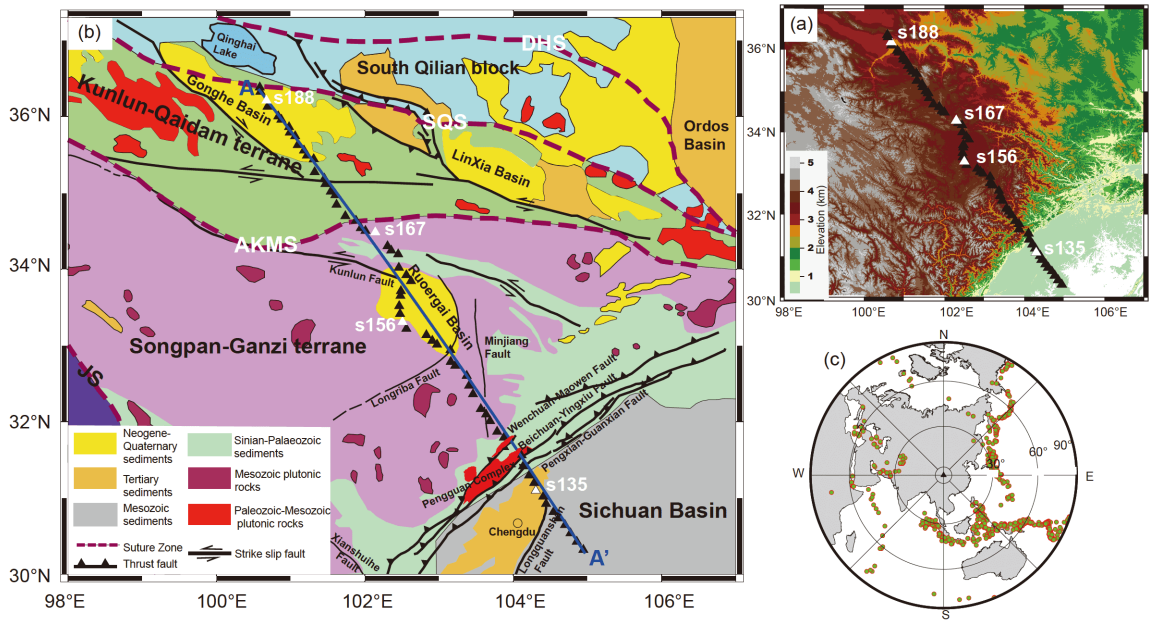

Figure 3 Topographic (a) and simplified tectonic maps (b) of the study region and distribution of teleseismic events (c). The black and white triangles in ((a), (b)) denote the location of broadband seismic stations. In (b), the blue solid line AA′ delineates the imaging profile. AKMS: Anyimaqen-Kunlun-Muztagh suture; SQS: South Qilian suture; DHS: Danghe Nanshan suture; JS: Jinsha river suture.

in the *j*th subspace, respectively; σ_j is the standard deviation of the amplitudes in the *j*th subspace; and $F_{i,j}\left(V_{S_0}, p_{i,j}\right)$ and $y_{i,j}$ represent the observed and synthetic amplitudes, respectively, in the *i*th receiver function with a ray parameter of $p_{i,j}$ in the *j*th subspace. A grid search method was performed to obtain the best-fit S-wave velocity by minimizing the residuals $\| \delta \|$ (Appendix Figure S1, http://earth.scichina.com). In this study, the S-wave velocity ranged from 1.0 to 5.0 km s^{-1}, and the search step was 0.001 km s^{-1}. Figure 4c shows the amplitude distribution of direct P-waves as a function of the ray parameter at station s167 for a Gaussian factor of 3.0. The best-fit S-wave velocity is 2.79 km s^{-1}, and the corresponding fitting curve is shown as a black solid line in Figure 4c. When the Gaussian factor is 3.0 and 5.0, i.e., frequencies of 0.95 and 1.60 Hz, respectively, the best-fit S-wave velocity at station s188 differs greatly (Figure 4e and 4f). Specifically, the velocity associated with the high frequency (1.96 km s^{-1}) is much lower than that associated with the low frequency (2.63 km s^{-1}).

Due to the presence of noise and/or the limited observation period, the number of observed receiver functions is typically small. We then conducted a bootstrap analysis to examine the observed S-wave velocity errors (Efron and Tibshirani, 1993). Figure 4d shows the bootstrapping results of station s167 for a Gaussian factor of 3.0. Two times the standard deviation is approximately 0.06 km s^{-1}, within which the velocity is considered to be within the 95% confidence level. Adequate searching for velocities requires data over a broad distance. In regions with poor data coverage, the application of eq. (5) may produce large uncertainties. In such regions, it may still be possible to constrain the velocities using eq. (1) with an average amplitude and ray parameter.

Based on the direct P-wave amplitudes at different frequencies, multiple S-wave velocity values were extracted, forming a velocity-period curve for each station (Figure 5). The velocity-period curves of individual tectonic units in our study region are clearly different. For example, station s167 shows weak velocity variations with period, whereas station s188 shows that the velocity increases markedly with increasing period, similar to that of positive-gradient- or even stepped-type models.

4. Results and discussion

The velocity-period curves were converted to the depth domain through an empirical correlation between frequency and depth (eq. (4)), in which a regional crustal V_P/V_S ratio of 1.77 from the *H*-κ results was used (Wang et al., 2018). We constructed the 2-D S-wave velocity images along the NW-SE line depicted in Figure 3a by interpolation. The velocity structures were imaged at depths between ~1.5 and ~7.0 km. Figure 6a and 6b show the S-wave velocity images constructed using the amplitude set for a single station and three nearby stations, respectively. Two times the standard deviation of the single-station S-wave velocities (Figure 6a) based on bootstrapping is generally less than 0.10 km s^{-1} (Figure 6c), suggesting that the results are reliable.

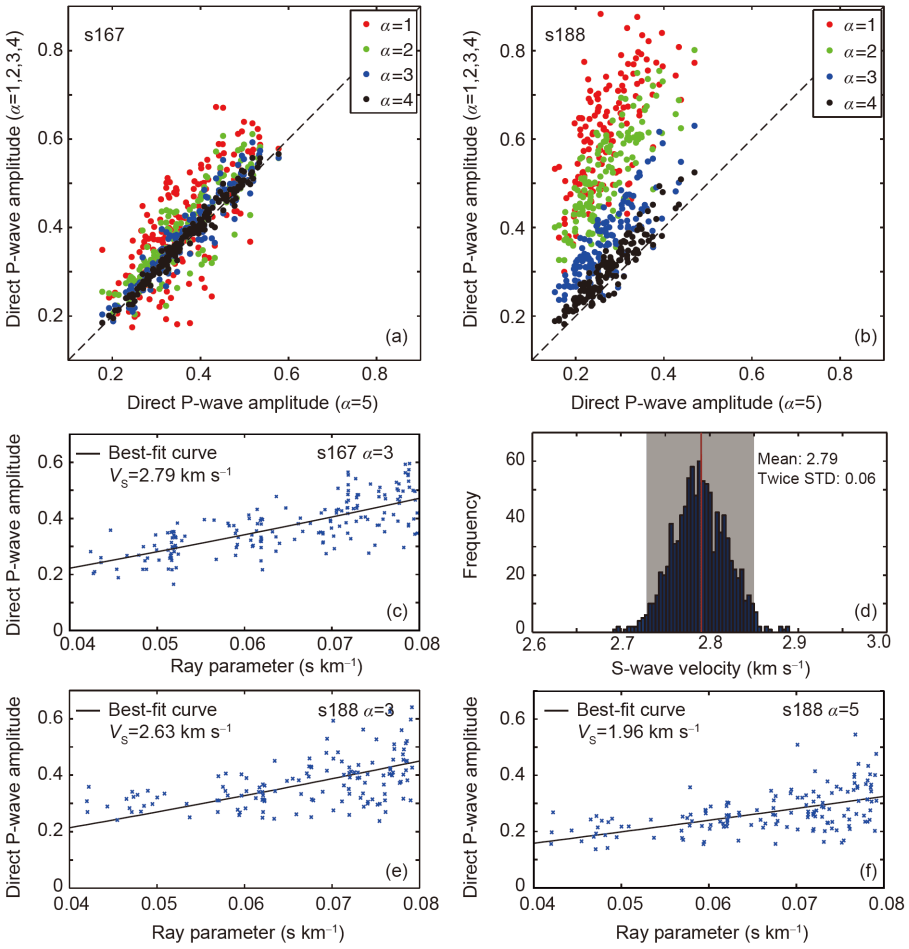

Figure 4 Amplitude variations of direct P-waves as a function of frequency ((a), (b)) and ray parameter ((c), (e), (f)) at representative stations and the histogram of the best-fit velocities by bootstrapping (d). In ((a), (b)), the red, green, blue and black dots represent the direct P-wave amplitudes with Gaussian factors of 1.0, 2.0, 3.0, and 4.0, respectively (ordinate axis) compared to the results for a Gaussian factor of 5.0 (abscissa axis). In ((c), (e), (f)), the black solid lines delineate the best-fit curve based on eq. (1), and the corresponding S-wave velocity is noted in the upper left of each figure.

4.1 Reliability analysis of the results

Differences in modelling techniques and parameterizations inevitably lead to waveform variations, especially the amplitudes of receiver functions. To some extent, such differences affect the stability of our results. Thus, we performed a series of tests by changing the calculation methods and parameters to evaluate this effect. The results suggest that based on existing data in this study, the standard deviation of the S-wave velocity differences among the different methods or parameters is less than 10% (Appendix Figures S2, S3a, S3b, and Table S1). Considering the large velocity variations within our study area (from 1.5 to 4 km s^{-1}), the range in relative velocity variations with respect to the regional average is approximately $\pm\left(\frac{4.0-1.5}{2}\right)/\left(\frac{4.0+1.5}{2}\right)\approx\pm45\%$. This value is obviously larger than the standard deviation of the velocity differences obtained using different calculating techniques or parameters (Appendix Table S1), suggesting that the obtained velocity structures are robust. Given the S-wave velocity, the P-wave wavelength can be estimated by knowing the V_P/V_S ratio (eq. (3)). Using the region-averaged or a more accurate single-station V_P/V_S ratio to estimate the wavelength can improve depth constraints. In this study, the velocity structure constructed with the region-averaged V_P/V_S ratio shows a pattern similar to that with the single-station V_P/V_S ratio. We conclude that it is feasible to use the amplitudes of teleseismic body waves to constrain shallow structures near a receiver, and this method has great potential in passive-source applications.

To further verify the reliability of the results produced by the new method, a neighbourhood algorithm method (NA; Sambridge, 1999a, 1999b) was applied to determine the S-wave velocities beneath individual stations. The model parameters used for waveform inversion are shown in Table 1. The receiver function waveforms from 2 s before to 3 s after the direct P-wave arrival contain a wealth of information on the shallow crust; therefore, the cross-correlation

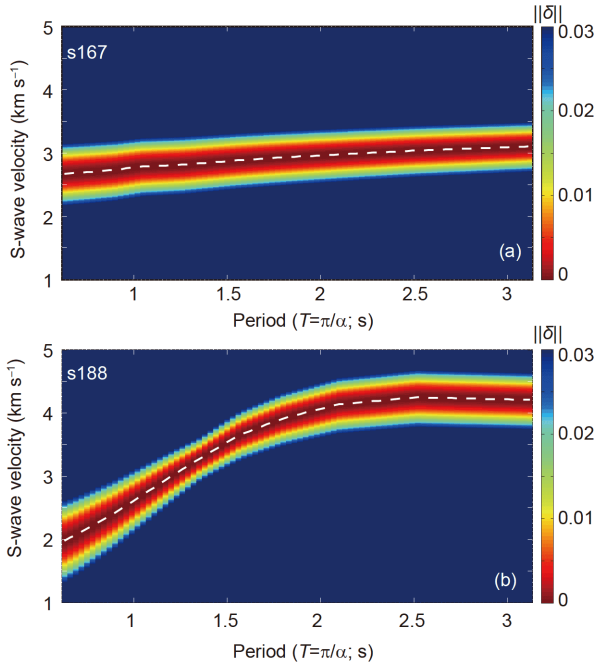

Figure 5 Distribution of normalized residual errors and extracted velocity-period curves (white dashed lines).

between the synthetic and observed waveforms within this window was calculated during the inversion. The inversion started with 100 random samples from the model space. Subsequently, 2000 iterations were carried out, and in each iteration, 20 models were resampled from 10 models with the lowest misfit of all models generated thus far. For each station, the inversion generated a total of 40100 models. The final result is represented by the mean of the 1000 best-fit models rather than a single best-fit model, as exemplified in Figure 7a and 7b. The observed receiver functions show good consistency in terms of the waveforms based on the best-fit model (Figure 7c and 7d). Considering both the signal-to-noise ratios and the resolution of the data, we inverted the receiver functions with Gaussian factors of 2.0 and 3.0 for the S-wave velocities.

The inverted velocity structures along the profile (Figure 8b and 8c) are in good agreement with those determined by the new method, such as low velocities beneath the Sichuan Basin and high velocities beneath the Gonghe Basin. However, there are some subtle differences between the velocity structures determined via the two methods. The velocity structures based on the waveform inversion technique at two different frequencies are also different. For example, the depth of the high-velocity anomaly beneath the Longmenshan area increases with decreasing frequency. Due to the usage of multiple-frequency amplitudes, the anomaly imaged by the new method identifies high velocities at both shallow and deep depths, thereby suggesting that the newly developed method effectively compensates for the deficiency of single-frequency waveform inversions. Our observations are consistent with the P-wave velocity variations reported from a wide-angle reflection and refraction study (Figure 8d). In addition, the synthetic waveforms of the direct P-waves fit well with those observed at individual frequencies (Figure 9). All of the comparisons and tests suggest

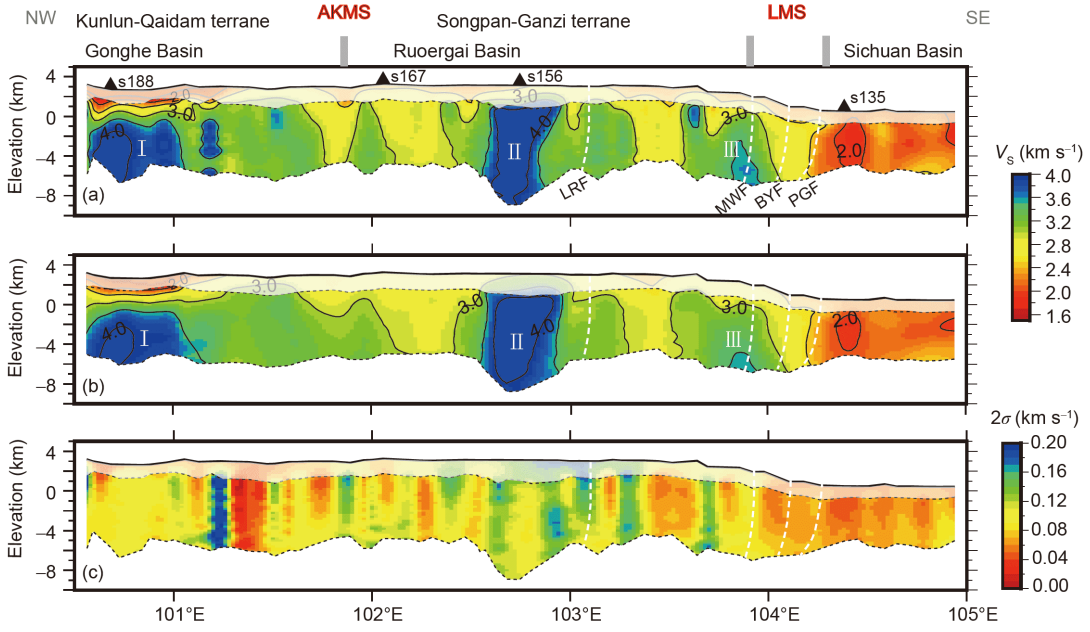

Figure 6 S-wave velocity images of the shallow crust ((a), (b)) and two times the standard deviation (c). (a) and (b) were constructed using the amplitude set for a single station and three adjacent stations, respectively. In (a)–(c), the black dashed lines delineate the effective depth range, the white dashed lines denote faults along the profile, and the white-masked area indicates the unsampled region, i.e., the S-wave velocities were estimated by extrapolation. In (a) and (b), I, II, and III mark the high-velocity anomalies. Abbreviations in (a): AKMS, Anyimaqen-Kunlun-Muztagh suture; LRF, Longriba fault; LMS, Longmenshan fault belt; MWF, Maoxian-Wenchuan fault; BYF, Beichuan-Yingxiu fault; PGF, Pengxian-Guanxian fault.

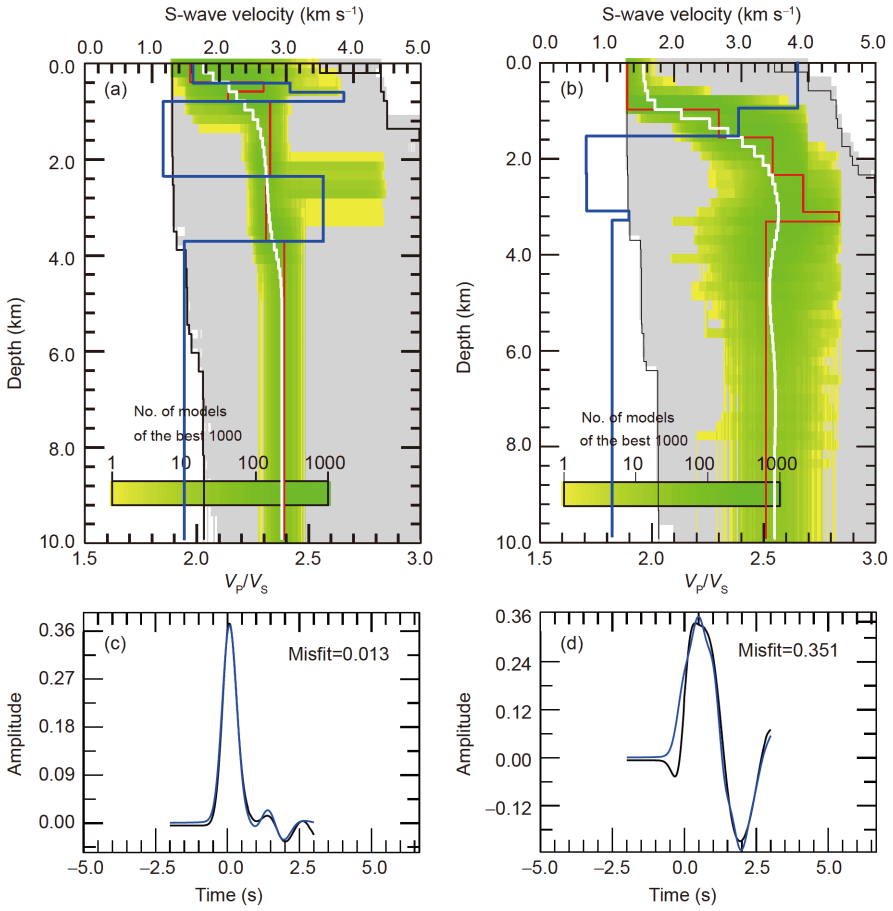

Figure 7 Inversion results based on the NA method (Sambridge, 1999a, 1999b) at stations s167 (left) and s188 (right). The results from receiver functions with a Gaussian factor of 3.0 are shown in the upper panels; below each panel is the corresponding observed (black lines) and synthetic (blue lines) receiver functions. The synthetics are based on the best-fit model shown as red lines in ((a), (b)). Each panel on top contains the entire model space (between two black lines), all generated models (grey lines), the best-fit model (red lines), V_P/V_S ratios (blue lines), and the mean of the 1000 best-fit models (white lines).

Table 1 Model space for NA inversion

Layer	Thickness (km)	Upper boundary V_S (km s^{-1})	Lower boundary V_S (km s^{-1})	V_P/V_S ratio
1	0–2	1.3–3.5	1.3–3.5	1.5–3.0
2	0–2	1.3–3.5	1.3–3.5	1.5–3.0
3	0–2	1.5–4.0	1.5–4.0	1.6–2.5
4	0–2	1.5–4.0	1.5–4.0	1.6–2.5
5	0–2	1.7–4.5	1.7–4.5	1.6–2.5
6	0–2	1.7–4.5	1.7–4.5	1.6–2.5
7	0–2	2.0–4.5	2.0–5.0	1.7–2.2

that the new method using frequency-dependent amplitudes of direct P-waves in P-RFs can effectively constrain the velocity structures in shallow crust.

4.2 S-wave velocity structures in the shallow crust

Figure 8a shows distinct variations in the S-wave velocities across the Longmenshan fault belt, which acts as the tectonic boundary between the Tibetan Plateau and the Sichuan Basin. The Sichuan Basin shows weak heterogeneous, low-velocity anomalies (with an average of ~2.1 km s^{-1}) that are closely related to the weak sedimentary layers in the basin. The average velocity beneath the Songpan-Ganzi terrane increases from ~2.9 km s^{-1} at ~1.5 km depth to ~3.2 km s^{-1} at ~7.0 km depth. Similar variations are observed beneath the Kunlun-Qaidam terrane with a velocity of ~2.6 km s^{-1} at ~1.5 km depth to ~3.3 km s^{-1} at ~7.0 km depth. Despite similar velocities at deep depths, the velocity of the Kunlun-Qaidam terrane at shallow depths is slightly lower than that of the Songpan-Ganzi terrane because of the presence of

significant low-velocity sediments in the Gonghe Basin.

Along the target profile (AA′ in Figure 3b), the imaged velocity variations at shallow depths are consistent with the surficial geology with low-velocity anomalies in basins, whereas high-velocity anomalies appear in mountains (Figure 6a and 6b). The sedimentary structures are quite different among the Sichuan, Ruoergai and Gonghe Basins, although all of them show low velocities. The low-velocity anomaly extends downwards to a depth of ~5 km beneath the Sichuan Basin, indicating that the crystalline basement is deeper than ~5 km. Instead, the low-velocity anomaly beneath the Gonghe Basin contacts with the high-velocity one at depths of ~2–3 km where the velocity increases rapidly from ~2.4 to ~3.2 km s^{-1} (I in Figure 6a). The shallow sediments of the Ruoergai Basin exhibit substantially higher S-wave velocities than those of the Sichuan and Gonghe Basins. At a depth of ~7 km, the velocity reaches approximately 3.2 km s^{-1}. Between the Ruoergai Basin and the Sichuan Basin, the shallow crust is characterized by a 'high-low-high' velocity pattern. Two high-velocity anomalies appear beneath the area west of the Longriba fault (II in Figure 6a) and the area west of the Longmenshan fault belt (III in Figure 6a). Their average S-wave velocities are ~4.0 km s^{-1} and ~3.3 km s^{-1}, respectively. Regions between the two high-velocity anomalies have similar velocity features to those of the Ruoergai Basin. The southern part of the Kunlun-Qaidam terrane is characterized by relatively high velocities compared to the Ruoergai Basin, and this region clearly separates the Gonghe Basin from the Ruoergai Basin.

4.3 Sedimentary and tectonic environments

The shallow crust of the Sichuan Basin and basins within the Tibetan Plateau have distinct S-wave velocity structures, probably reflecting different sedimentary and tectonic environments. Geophysical studies have revealed thick Precambrian to Cenozoic sediments (6–15 km; Gao et al., 2016; Mei et al., 2014), laterally homogeneous crust (Wang et al., 2018) and thick, high-velocity lithosphere beneath the Sichuan Basin (Zhang et al., 2018; Lei and Zhao, 2016), in-

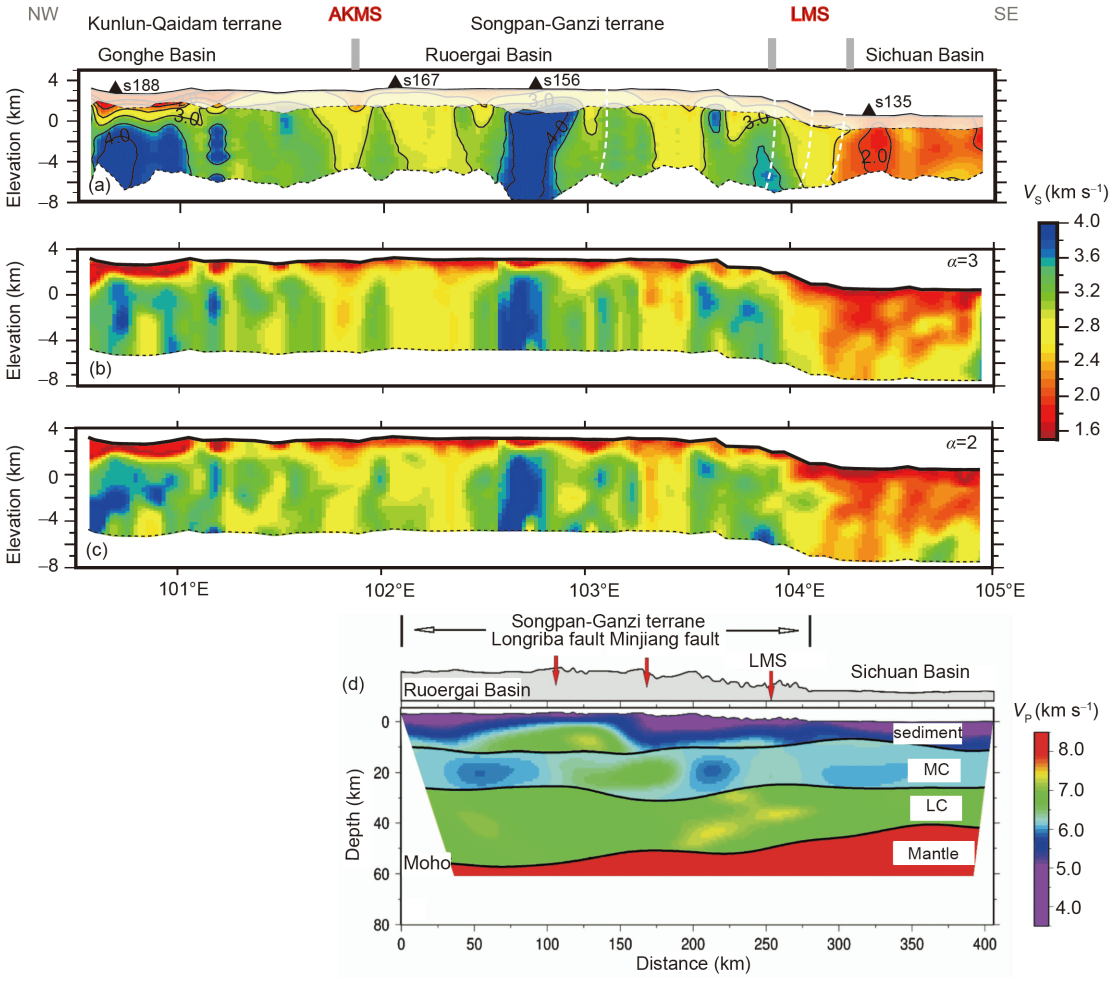

Figure 8 Comparison of velocity structures along the AA′ profile. The S-wave velocity structures were constructed by the new method (a) and by inversion of the receiver functions with Gaussian factors of 3.0 (b) and 2.0 (c). The P-wave velocity structures (d) are from a wide-angle reflection and refraction study (Xu et al., 2016). Abbreviations on top are the same as those in Figure 6. MC and LC in (d) represent the middle and the lower crust, respectively.

dicating that this area has remained rigid and stable and has retained the characteristics of a typical craton. The shallow crust of the Sichuan Basin is imaged as low velocities with weak lateral variations, which may be the result of long-term stable sedimentation in the Mesozoic and Cenozoic. P-RF migration images along the AA' profile (Wang et al., 2018) show that the crust in the Tibetan region is thick and that crustal structures such as the crystalline basement exhibit obvious lateral variations, indicating that the crust of eastern and northeastern Tibet has undergone intense compression and thickening in response to the Cenozoic Indian-Eurasian collision (Jia et al., 2014; Guo et al., 2013; Li et al., 2011; Wang et al., 2011; Wang et al., 2016; Zhao et al., 2012). In contrast to the thick and relatively high velocity sediments in the Ruoergai Basin, the sediments in the Gonghe Basin are thin (<3 km) and underlain by a high-velocity anomaly. The differences in sedimentary thickness and seismic wave velocity between the two plateau basins reflect the complexity of sedimentary characteristics in compressional environments.

The three high-velocity anomalies beneath eastern and northeastern Tibet may be related to the Palaeozoic-Cenozoic multi-stage acidic magma intrusion and/or the Cenozoic Indian-Eurasian continental collision. As a main component of eastern Tibet, the Songpan-Ganzi terrane is widely covered by thick Triassic strata, namely, the Triassic flysch complex (Nie et al., 1994; Zhou and Graham, 1996). There are Permian to Cenozoic acidic igneous rocks in the interior of the terrane (Bureau of Geology and Mineral resources of Sichuan Province, 1991). Proterozoic strata mostly outcrop in the marginal area of the terrane, such as the Xuelongbao metamorphic complex in the Longmenshan area (Zhou et al., 2006). Active-source seismic profiles (Hubbard and Shaw, 2009; Li et al., 2010) and P-RF migration images (Wang et al., 2018) show that the brittle upper crust of the Songpan-Ganzi terrane has been thrust over the basement of the Sichuan Basin in the Longmenshan area. The high-velocity anomaly observed beneath the region west of the Longmenshan fault may be associated with uplifted basement and a thrust nappe (Zhang et al., 2017). The high-V_S body beneath the region west of the Longriba fault is consistent in location with a high-V_P and high-density anomaly revealed by the wide-angle reflection, refraction, and gravity study (Xu et al., 2016). The high-V_P and high-density anomaly is considered to be related to the intrusion of adakitic granite formed by partial melting of the Proterozoic basement in the Mesozoic (Zhang et al., 2006). Our results (Figures 6a and 8a–8c), however, show that the S-wave velocities of the anomalous body are slightly higher than 4.0 km s^{-1}, which are markedly higher than the S-wave velocity of granitoids. The waveform comparison result at station s156 shows that the simulated direct P-wave amplitudes are in agreement with the observed at individual frequencies, although the arrival time differs, especially at relatively high frequencies (Figure 9b). This result suggests the presence of more complex structures in this area than modelled by this study. Therefore, further study or logging data are required to verify the existence of a high-velocity anomaly and whether it represents a granitic intrusion.

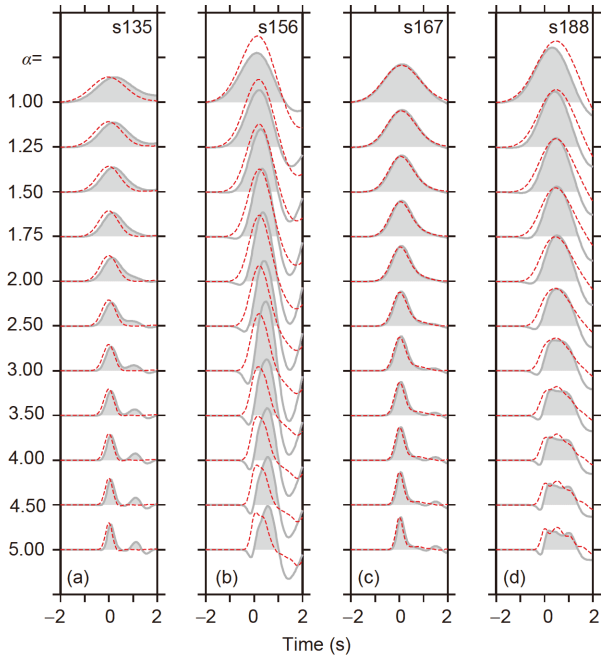

Figure 9 Comparison of the synthetic (red dashed lines) and the observed (grey shadow) P-wave receiver functions. The station locations and velocity models are shown in Figure 6a.

In recent years, the Gonghe Basin has received more attention because of the high geothermal potential. Geophysical exploration results show that the Gonghe Basin has a shallow basement (1–3 km; Wang et al., 2010) composed of Indo-Sinian granites. Geothermal drilling data reveal that the basin is characterized by a high geothermal gradient, and the heat source is considered to be related to deep-seated granite bodies (Xue et al., 2013). The transition from low to high velocities in our observations could signify the basin basement, the depth of which is less than 3 km. The high-velocity body beneath the sediments likely represents the spatial distribution of granitoids (dry hot rocks), which indicates good geothermal development potential in this area.

5. Conclusions

We developed a method to constrain S-wave velocities in the shallow crust with frequency-dependent amplitudes of direct P-waves in P-RFs. Unlike traditional inversions that often use a single frequency waveform, the newly developed method reduces the nonuniqueness of solutions and constrains the shallow structure due to the usage of multi-fre-

quency amplitudes. The main objective of this paper was to demonstrate the feasibility of high-resolution imaging of the shallow crust beneath receivers using the teleseismic recordings.

An S-wave velocity image of the shallow crust along one section of eastern and northeastern Tibet was obtained using the new method. New observations reveal different structures on both sides of the Longmenshan fault zone, the tectonic boundary between the Tibetan Plateau and the Sichuan Basin. The Sichuan Basin and basins within Tibet show distinct S-wave velocity structures in the shallow crust, indicating different sedimentary characteristics. The shallow crust of the Sichuan Basin exhibits uniform low-velocity structures, consistent with the sedimentary characteristics of an ancient, stable cratonic basin. As a result of intense responses of shallow crust to the Cenozoic Indian-Eurasian collision, the S-wave velocities in the Longmenshan and Tibetan region are relatively high and show strong inhomogeneity compared to that of the Sichuan Basin. Three distinct high-velocity anomalies appear in the shallow crust of the plateau along the target profile. The anomaly beneath the area west of the Longmenshan fault belt may be related to the nappe-related uplift of the Proterozoic basement, while those beneath the areas west of the Longriba fault and the Gonghe Basin may be related to the emplacement of Palaeozoic-Mesozoic intrusive rocks.

Acknowledgements *The teleseismic three-component recordings were provided by the Seismic Array Laboratory of IGGCAS (doi:10.12129/IGGSL.Data.Observation, http://www.seislab.cn/). We thank the two anonymous reviewers and editors for their constructive comments and suggestions, which significantly improved the manuscript. This research was supported by the National Natural Science Foundation of China (Grant No. 41688103), the Strategic Priority Research Program (A) of the Chinese Academy of Sciences (Grant No. XDA20070302) and the Independent Project of the State Key Laboratory of the Lithospheric Evolution, IGGCAS (SKL-Z201704-11712180). The field work for seismic data collection was financially supported by the Projects (Grant Nos. SinoProbe-02-03, 2011ZX05008-001).*

References

Ai Y S, Zheng T Y, Xu W W, He Y M, Dong D. 2003. A complex 660 km discontinuity beneath northeast China. Earth Planet Sci Lett, 212: 63–71
Ammon C J, Randall G E, Zandt G. 1990. On the nonuniqueness of receiver function inversions. J Geophys Res, 95: 15303–15318
Arai H, Tokimatsu K. 2004. S-wave velocity profiling by inversion of microtremor H/V spectrum. Bull Seismological Soc Am, 94: 53–63
Bostock M G. 1999. Seismic waves converted from velocity gradient anomalies in the Earth's upper mantle. Geophys J Int, 138: 747–756
Bostock M G, Rondenay S. 1999. Migration of scattered teleseismic body waves. Geophys J Int, 137: 732–746
Bureau of Geology and Mineral resources of Sichuan Province. 1991. Regional Geology of Sichuan Province. Beijing: Geological Publishing House. 1–732
Chen L, Wen L, Zheng T. 2005a. A wave equation migration method for receiver function imaging: 1. Theory. J Geophys Res, 110: B11309
Chen L, Wen L, Zheng T. 2005b. A wave equation migration method for receiver function imaging: 2. Application to the Japan subduction zone. J Geophys Res, 110: B11310
Chen L, Zheng T, Xu W. 2006. Receiver function migration image of the deep structure in the Bohai Bay Basin, eastern China. Geophys Res Lett, 33: L20307
Clark M K, Royden L H. 2000. Topographic ooze: Building the eastern margin of Tibet by lower crustal flow. Geology, 28: 703–706
Dueker K G, Sheehan A F. 1997. Mantle discontinuity structure from midpoint stacks of converted P to S waves across the Yellowstone hotspot track. J Geophys Res, 102: 8313–8327
Efron B, Tibshirani R J. 1993. An Introduction to the Bootstrap. Chapman and Hall
Fang H, Yao H, Zhang H, Huang Y C, van der Hilst R D. 2015. Direct inversion of surface wave dispersion for three-dimensional shallow crustal structure based on ray tracing: Methodology and application. Geophys J Int, 201: 1251–1263
Gao R, Chen C, Wang H, Lu Z, Brown L, Dong S, Feng S, Li Q, Li W, Wen Z, Li F. 2016. SINOPROBE deep reflection profile reveals a Neo-Proterozoic subduction zone beneath Sichuan Basin. Earth Planet Sci Lett, 454: 86–91
Guo X, Gao R, Randy Keller G, Xu X, Wang H, Li W. 2013. Imaging the crustal structure beneath the eastern Tibetan Plateau and implications for the uplift of the Longmen Shan range. Earth Planet Sci Lett, 379: 72–80
Hubbard J, Shaw J H. 2009. Uplift of the Longmen Shan and Tibetan plateau, and the 2008 Wenchuan (M=7.9) earthquake. Nature, 458: 194–197
Jia S X, Liu B J, Xu Z F, Liu Z, Feng S Y, Zhang J S, Lin J Y, Tian X F, Liu Q X, Guo W B. 2014. The crustal structures of the central Longmenshan along and its margins as related to the seismotectonics of the 2008 Wenchuan Earthquake. Sci China Earth Sci, 57: 777–790
Julià J. 2007. Constraining velocity and density contrasts across the crust-mantle boundary with receiver function amplitudes. Geophys J Int, 141: 286–301
Kennett B L N. 1983. Seismic Wave Propagation in Stratified Media. Cambridge: Cambridge University Press. 1–342
Lei J, Zhao D. 2016. Teleseismic P-wave tomography and mantle dynamics beneath Eastern Tibet. Geochem Geophys Geosyst, 17: 1861–1884
Li Y, Jia D, Shaw J H, Hubbard J, Lin A M, Wang M M, Luo L, Li H B, Wu L. 2010. Structural interpretation of the coseismic faults of the Wenchuan earthquake: Three-dimensional modeling of the Longmen Shan fold-and-thrust belt. J Geophys Res, 115: B04317
Li Z W, Xu Y, Huang R Q, Hao T Y, Xu Y, Liu J S, Liu J H. 2011. Crustal P-wave velocity structure of the Longmenshan region and its tectonic implications for the 2008 Wenchuan earthquake. Sci China Earth Sci, 54: 1386–1393
Liu Q Y, Kind R, Li S C. 1996. Maximal likelihood estimation and nonlinear inversion of the complex receiver function spectrum ratio (in Chinese). Chin J Geophys, 9: 500–511
Mei Q H, He D, Wen Z, Li Y. 2014. Geologic structure and tectonic evolution of Leshan-Longnvsi paleo-uplift in Sichuan Basin (in Chinese). Acta Petrol Sin, 35: 11–25
Nie S, Yin A, Rowley D B, Jin Y. 1994. Exhumation of the Dabie Shan ultra-high-pressure rocks and accumulation of the Songpan-Ganzi flysch sequence, central China. Geology, 22: 999–1002
Owens T J, Zandt G, Taylor S R. 1984. Seismic evidence for an ancient rift beneath the Cumberland Plateau, Tennessee: A detailed analysis of broadband teleseismic P waveforms. J Geophys Res, 89: 7783–7795
Qian Y P, Shen X Z, Li C Q, Mei X P, Jiao Y Y. 2018. Constraining the subsurface S-wave velocity of the northeastern margin of Tibetan Plateau with receiver functions (in Chinese). Chin J Geophys, 61: 3951–3963
Sambridge M. 1999a. Geophysical inversion with a neighbourhood algorithm-I. Searching a parameter space. Geophys J Int, 138: 479–494
Sambridge M. 1999b. Geophysical inversion with a neighbourhood algorithm-II. Appraising the ensemble. Geophys J Int, 138: 727–746
Tapponnier P, Xu Z, Roger F, Meyer B, Arnaud N, Wittlinger G, Jingsui Y. 2001. Oblique stepwise rise and growth of the Tibet plateau. Science,

294: 1671–1677
Wang B, He S H, Li B X, Song Y D. 2010. Geothermal resource distribution characteristics of Gonghe basin in Qinghai-Effect of CSAMT in geothermal prospecting (in Chinese). Mineral Res Geol, 24: 279–285
Wang C S, Gao R, Yin A, Wang H Y, Zhang Y, Guo T, Li Q, Li Y. 2011. A mid-crustal strain-transfer model for continental deformation: A new perspective from high-resolution deep seismic-reflection profiling across NE Tibet. Earth Planet Sci Lett, 306: 279–288
Wang H Y, Gao R, Zhang J S, Li Q S, Guan Y, Li W H, Guo X Y, Li H Q. 2016. Research of the crustal property of the Songpan-Garze block (in Chinese). Chin J Geol, 51: 41–52
Wang X, Chen L, Ai Y S, Xu T, Jiang M M, Ling Y, Gao Y F. 2018. Crustal structure and deformation beneath eastern and northeastern Tibet revealed by P-wave receiver functions. Earth Planet Sci Lett, 497: 69–79
Wu Q J, Zeng R S. 1998. The crustal structure of Qinghai-Xizang plateau inferred from broadband teleseismic waveform (in Chinese). Chin J Geophys, 41: 669–679
Wu Q J, Tian X B, Zhang N L, Li W P, Zeng R S. 2003. Receiver function estimated by maximum entropy deconvolution (in Chinese). Acta Seismol Sin, 25: 382–389
Xu X, Gao R, Guo X Y, Keller G R. 2016. The crustal structure of the Longmenshan Shan and adjacent regions: An integrated analysis of seismic profiling and gravity anomaly (in Chinese). Chin J Geol, 51: 26–40
Xue J Q, Gan B, Li B X, Wang Z L. 2013. Geological-geophysical characteristics of enhanced geothermal systems (hot dry rocks) in Gonghe-Guide Basin (in Chinese). Geophys Geochem Explor, 37: 35–41
Yang Y, Yao H, Zhang P, Chen L. 2018. Crustal azimuthal anisotropy in the trans-North China orogen and adjacent regions from receiver functions. Sci China Earth Sci, 61: 903–913
Yin A, Harrison T M. 2000. Geologic evolution of the Himalayan-Tibetan orogen. Annu Rev Earth Planet Sci, 28: 211–280
Yuan Y, Yao H J, Qin Y. 2016. Joint inversion of Rayleigh wave vertical-horizontal amplitude ratios and dispersion based on the Neighborhod Algorithm and its application (in Chinese). Chin J Geophys, 59: 959–971
Zhang H F, Zhang L, Harris N, Jin L L, Yuan H. 2006. U–Pb zircon ages, geochemical and isotopic compositions of granitoids in Songpan-Garze fold belt, eastern Tibetan Plateau: Constraints on petrogenesis and tectonic evolution of the basement. Contrib Mineral Petrol, 152: 75–88
Zhang X Y, Wang Y H, Gao R, Xu T, Bai Z M, Tian X B, Li Q S. 2017. Vertical crustal motions across Eastern Tibet revealed by topography-dependent seismic tomography. Sci Rep, 7: 3243
Zhang Y Y, Chen L, Ai Y S, Jiang M M, Xu W W, Shen Z Y. 2018. Lithospheric structure of the South China Block from S-receiver function (in Chinese). Chin J Geophys, 61: 138–149
Zhang Z J, Wang Y H, Chen Y, Houseman G A, Tian X B, Wang E, Teng J W. 2009. Crustal structure across Longmenshan fault belt from passive source seismic profiling. Geophys Res Lett, 36: 1397
Zhang Z J, Yuan X H, Chen Y, Tian X B, Kind R, Li X Q, Teng J W. 2010. Seismic signature of the collision between the east Tibetan escape flow and the Sichuan basin. Earth Planet Sci Lett, 292: 254–264
Zhao G Z, Unsworth M J, Zhan Y, Wang L F, Chen X B, Jones A G, Tang J, Xiao Q B, Wang J J, Cai J T, Li T, Wang Y Z, Zhang J H. 2012. Crustal structure and rheology of the Longmenshan and Wenchuan M_W7.9 earthquake epicentral area from magnetotelluric data. Geology, 40: 1139–1142
Zheng T Y, Chen L, Zhao L, Xu W W, Zhu R X. 2006. Crust–mantle structure difference across the gravity gradient zone in North China Craton: Seismic image of the thinned continental crust. Phys Earth Planet Inter, 159: 43–58
Zhou D, Graham S A. 1996. Songpan-Ganzi Triassic flysch complex of the West Qinling Shan as a remnant ocean basin. In: Yin A, Harrison M. (Eds.), The Tectonic Evolution of Asia. Cambridge: Cambridge University Press. 281–299
Zhou M F, Yan D P, Wang C L, Qi L, Kennedy A. 2006. Subduction-related origin of the 750 Ma Xuelongbao adakitic complex (Sichuan Province, China): Implications for the tectonic setting of the giant Neoproterozoic magmatic event in South China. Earth Planet Sci Lett, 248: 286–300
Zhu L, Kanamori H. 2000. Moho depth variation in southern California from teleseismic receiver functions. J Geophys Res, 105: 2969–2980

(Responsible editor: Huaiyu YUAN)